A force-limiting mechanism for needle insertions

A. Aktas, E. Franco

***Abstract*—Needle bending is a significant cause of error in biopsies, leading to lesion missampling and consequent cancer misdiagnosis. This paper presents the design of a new mechanism that detects the needle bending as soon as it occurs and immediately reduces the insertion force. Importantly, this is achieved without employing external sensors or electromechanical actuators. Experiments on a silicone-rubber phantom indicate that the proposed device can help to avoid deep insertions with bent needles, thus potentially reducing the associated risks and improving patient safety in biopsies and percutaneous interventions.**

***Index Terms*—Needle insertion, Needle bending, Mechanism design, Medical robotics, Minimally invasive surgery.**

I. Introduction

OVER 1 million core-needle breast biopsies are performed every year in the US alone [1], while gastrointestinal and prostate biopsies are estimated in similar numbers. The cost of core-needle breast biopsies ranges between $500 for manual procedures to $6,000 for image-guided procedures [2]. A retrospective study indicated that approximately 2.5% of breast biopsies fail [3]. Needle bending has been identified as a significant cause of error in biopsies [4], and it is particularly likely to occur at the insertion stage [2]. The associated risks include: i) biopsy of the wrong site leading to misdiagnosis; ii) puncture of sensitive areas in close proximity of the insertion path; iii) repeated insertions, thus longer procedure duration and increased patient discomfort. Biopsy needles are also prone to buckling, which can damage the needle permanently. Besides biopsy, needle insertion is common to various percutaneous interventions, including image-guided brachytherapy [5] and image-guided laser ablation [6]. Extensive research has been conducted to model needle bending by employing beam theory or data-driven approaches [7], [8], [9], and to identify the mechanical properties of the soft tissues contributing to this phenomenon [10]. Recent works have also investigated the use of FBG sensors to estimate the shape of the needle during the insertion [11] and to measure the insertion force [12], [13]. While most needle insertions in clinical practice are conducted manually, various robotic solutions have been proposed to improve accuracy [14]. In parallel, training simulators have been developed to reduce the learning curve for clinicians [15].

Established solutions to correct needle bending that are routinely employed in clinical practice include: i) repeating the insertion, which is, however, time-consuming; ii) using a needle guide to minimize bending, which, however, reduces the maximum insertion depth. In literature, axial rotation is typically employed for steering bevel-tip needles [16], but it is less effective for needles with axial-symmetric tips [17]. Nevertheless, recent works indicate that multi-bevel needles might be better suited for biopsy compared to single-bevel needles [4]. Additionally, straight insertions with single-bevel needles require continuous axial rotation, which can damage soft tissues due to the spinning of the bevel tip. This undesirable effect can only be partially mitigated with bidirectional rotation strategies [18]. Alternative approaches employ actuated steerable needles [19] that are not yet part of clinical practice. In our previous work, we have proposed control algorithms that reduce the bending of multi-bevel needles by up to 70% in closed-loop insertions without employing axial rotation [20], [21]. However, the controllers require sensors and actuators hence they are not applicable to manual insertions.

In this paper, we present the design and the experimental evaluation of a novel mechanism for straight needle insertions that can detect needle bending as soon as it occurs, and that reduces the insertion force, thus preventing further bending (see Figure 1A). Since the mechanism does not employ sensors or actuators, it is MRI-compatible, it can be produced in low-resource settings, and it can be used with a variety of standard needles in open-loop manual procedures. The working principle of the mechanism is illustrated in Section II (see Figure 1B and Figure 1C), while the experimental results are presented in Section III.

II. Mechanism Design

A. System model

In our previous works [20], [21], we have shown that the dynamics of a slender metallic needle with mass m and length L can be described with a pseudo-rigid-body model as

$$m\ddot{q}_1 - ml\sin(q_2)\,\ddot{q}_2 - ml\cos(q_2)\,\dot{q}_2^2 = F, \qquad (1a)$$

$$-ml\sin(q_2)\,\ddot{q}_1 + ml^2\ddot{q}_2 + k_t q_2 + c_v\dot{q}_2 = 0, \qquad (1b)$$

where q_1 is the axial translation of the needle base, q_2 is the bending angle of the needle, $l = \gamma L$ is the length, $k_t = \gamma\kappa EI_0/L$ the bending stiffness, and c_v the natural damping, while F is the insertion force (see Figure 1D). The Young modulus E (i.e., $E = 100$ GPa for titanium) and the moment of inertia I_0 refer to the needle, while the parameters γ and κ ensure kineto-static equivalence with the pseudo-rigid-body model [22]. It follows from (1a), (1b) that the insertion force is related to the axial displacement q_1 and to the bending angle q_2 by the stiffness k_t and, to a lesser extent, by the damping c_v. Computing $\ddot{q}_2$ from (1b) at $\dot{q}_2 = 0$ for illustrative purposes, which corresponds to quasi-static conditions, yields

$$ml\ddot{q}_2 = m\sin(q_2)\ddot{q}_1 - q_2 k_t/l.$$

Substituting this expression in (1a) yields

$$m\ddot{q}_1\cos(q_2)^2 + \sin(q_2)q_2 k_t/l = F.$$

The authors are with Imperial College London, Mechanical Engineering Department, SW7 2AZ, UK. Email: e.franco11@imperial.ac.uk

This work has been supported by the Hamlyn Accelerator for Surgical Innovation, funded by the Wellcome Trust. The work of Ayhan Aktas was also supported by the Republic of Türkiye.

Thus, a larger needle bending q_2 (and corresponding deflection $\sigma = l\sin(q_2)$) stores elastic energy and reduces the effect of the insertion force in the axial direction. The aim of this work is to counteract this undesirable effect by reducing the insertion force as soon as the needle starts to bend.

B. Design implementation

The closed-loop controller presented in [20] reduces the insertion force produced by an actuator when needle bending is detected by an electromagnetic (EM) sensor. This feature is implemented in this work by a new force-limiting mechanism that reduces the insertion force applied by an operator in the presence of needle bending. The key difference from [20] is that the new mechanism does not require sensors, actuators, or a control algorithm hence it can be employed in open-loop manual procedures with standard needles.

The proposed device resembles a syringe in that it consists of a piston, used to impart the insertion force, and of a main body, which houses the force-limiting mechanism and supports the needle. A check valve is embedded in the piston to refill the internal chamber during retraction for repeated insertions. The force-limiting mechanism consists of a spring-loaded relief valve connected to the needle base. The working principle entails the following steps: i) when the needle bends, its base moves laterally and tilts the plunger of the relief valve; ii) this reduces the compression of the O-ring mounted on the plunger hence the internal pressure drops allowing the piston to advance towards the needle base (see Figure 1B and Figure 1C); iii) consequently, the insertion force is reduced, and the needle does not bend further. The design of the force-limiting mechanism is conducted by employing a kineto-static approach. The equilibrium to rotation for the plunger of the relief valve in the xy plane around the point C yields

$$F_s h = F\left(\frac{D_v}{D_c}\right)^2 \frac{D_o}{2} + \frac{k_t|q_2|}{L} H_v + E_o w \pi \frac{D_o}{4} h, \quad (2)$$

where $h = (\frac{D_o}{2} + \frac{2D_o}{3\pi})$ is the moment arm for the O-ring and spring, F_s is the spring force, and F is the insertion force transmitted by the piston of diameter D_c (i.e., $F = P\pi D_c^2/4$, with P the internal pressure). The parameters E_o, D_o and w are the Young modulus, mean diameter, and compression of the O-ring, while H_v is the length of the plunger, and D_v the orifice diameter of the relief valve. Note that the needle only transmits lateral forces to the valve plunger (see Figure 1E). If the needle remains straight (i.e., $q_2 = 0$), the equilibrium to translation of the plunger in the axial direction x yields

$$F_s = F\left(D_v/D_c\right)^2 + E_o w \pi D_o/2. \quad (3)$$

It follows from (2) and (3) that a higher spring force F_s results in a larger compression w of the O-ring. Therefore, the relief valve remains closed while larger insertion forces $F \geq 0$ are transmitted to the needle. Conversely, a rotation $q_2 \neq 0$ decompresses the O-ring causing the relief valve to open at lower pressures P, thus limiting the insertion force.

A prototype has been manufactured with standard 3D printing technologies, it is 172 mm long and weighs 85 grams. Two different springs have been mounted on the plunger of the relief valve separately for comparison purposes: Spring 1 (i.e., outer diameter 7.92 mm, length 19.05 mm, stiffness 0.03 N/mm); Spring 2 (i.e., outer diameter 7.92 mm, length 15.88 mm, stiffness 0.213 N/mm). To allow for further adjustment, the spring can be pre-tensioned by various amounts thanks to a threaded connection on the relief valve (see Figure 1E).

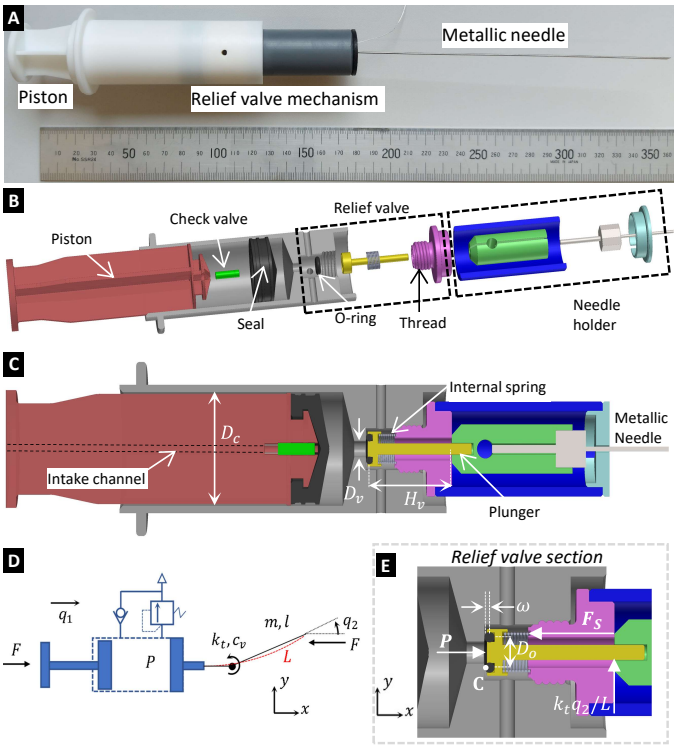

Fig. 1. Photo of the prototype (A), exploded view (B) and section view of the CAD model (C), schematic (D), and detail view of the relief valve (E).

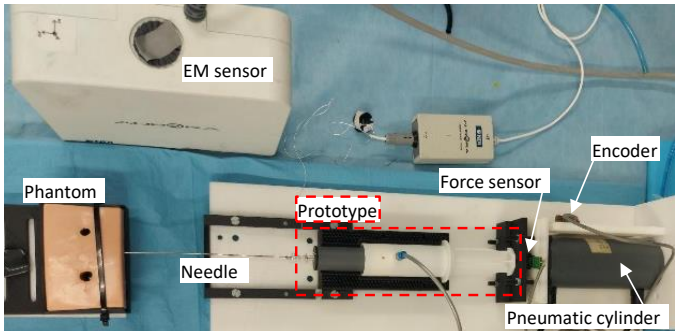

Fig. 2. Test setup for needle insertions in a silicone-rubber phantom.

C. Test setup

The test setup (see Figure 2) for needle insertions in a silicone rubber phantom employs a double-acting plastic pneumatic cylinder (AC111-707-501, IPS Inc.) supplied by digital pressure regulators (Tecno Basic, Hoerbiger, Germany). A PID algorithm has been employed to control the position of the pneumatic cylinder, which is measured with a linear encoder (EM1-300, US Digital). For data collection purposes, needle bending has been measured with an EM tracking system (Aurora, NDI Europe) by using an 18G coaxial titanium

TABLE I
EXPERIMENTAL RESULTS FOR SHORE A=10 PHANTOM

	Spring 1		**Spring 2**		**Fixed**	
	Bending Angle					
Speed [mm/s]	**4**	**8**	**4**	**8**	**4**	**8**
Mean q_2 [deg]	3.82	3.52	15.18	10.22	34.76	30.34
STD q_2 [deg]	1.11	0.43	3.39	2.87	7.45	6.33
	Axial Displacement					
Mean q_1 [mm]	59	60	59	60	44	49
STD q_2 [mm]	0.04	0.02	0.08	0.01	0.05	2.23
	Insertion Force					
Mean F [N]	1.46	0.83	2.62	1.96	0.75	1.35
STD F [N]	0.31	0.49	0.48	0.22	0.16	0.49

needle (1.3 mm OD, 0.8 mm ID, 150 mm long) instrumented with an EM sensor (part number 610061, NDI Europe, RMS accuracy 0.2 degrees). A force sensor (FSG15N1 A, Honeywell) mounted on the piston measures the insertion force. A micro-controller (mbed NXP LPC1768) communicates the pressure set-point to the digital regulators. A Matlab script logs data from the micro-controller and from the EM tracking system. Multiple needle insertions have been conducted with a silicone-rubber phantom (PlatSil GEL-10, Polytek), Shore A = 10, representative of liver tissues [23].

III. EXPERIMENTAL RESULTS

Each insertion has been repeated five times setting the needle perpendicular to the surface of the phantom. All results are shown in Figure 3 and are summarized in Table I. For each test, the mean (displayed in red) and the standard deviation (displayed in shaded blue) have been computed for axial displacement q_1, bending angle q_2, and insertion force F. The prescribed axial displacement $q_1 = 60$ mm corresponds to an insertion depth of approximately 30 mm. The first two columns of Figure 3 refer to Spring 1: in the first column the mean insertion speed is 4 mm/s, while in the second column it is 8 mm/s (i.e., the speed profile of the pneumatic cylinder has been obtained empirically by tuning the PID gains). Both speeds are representative of percutaneous interventions of the liver (see [24]). In general, faster insertions result in larger insertion forces and larger needle bending [24]. This is also the case without force-limiting mechanism (see columns "fixed" in Table I). Instead, the force-limiting mechanism results in comparable or slightly lower insertion forces at higher speed of insertion. The reason for this behavior is that the compressed air generated by the piston and vented though the relief valve introduces nonlinear damping [25], which become more noticeable at higher speed. The third column of Figure 3 shows a further set of results using Spring 2. In this case, the insertion force and the maximum bending angle reach higher values. This indicates that needle bending can be limited to a preset level by appropriately selecting the internal spring in the relief valve. In particular, the decision of whether a given needle bending is acceptable rests with the clinicians and depends on the specific percutaneous intervention. Computing the O-ring compression w from (2) at $q_2 = 10^\circ$ and $F = 2$ N (i.e., see fourth column in Table I) using Spring 2, $D_v = 4.13$ mm, $D_c = 30$ mm, $D_o = 6$ mm, $E_o = 2$ MPa for NBR (Nitrile), $H_v = 25$ mm, $L = 150$ mm and $k_t = 130$ Nmm/rad, yields approximately $w = 0.1$ mm. This value corresponds to the results of an FEA study of the loaded O-ring, and highlights the sensitivity of the mechanism to surface finish, which is typically limited when using 3D printing technologies, resulting in noticeable force variability (see Figure 3g). The fourth column of Figure 3 shows that removing the force-limiting mechanism yields bending angles $q_2 \approx 30^\circ$ and insertion forces $F \approx 1$ N (see the columns **Fixed** in Table I). Even though q_2 is much higher, the insertion force is not larger than with the force-limiting mechanism since the needle is buckling. Consequently, the mechanical work of the insertion force is employed to bend the needle, which applies a lateral force to the phantom. This behavior is characteristic of insertions where the needle is only supported at the base, as discussed in Section IIA. For the same reason, the standard deviation of the bending angle q_2 is larger in the last column of Table I. Note that in this case, the prescribed axial displacement has been reduced to $q_1 = 50$ mm to avoid permanent needle damage. Compared to this condition, the needle bending in the first two columns of Figure 3 is reduced by over 80%, which is similar to the results achieved with our controller [20] in automated closed-loop insertions. A video of the experiments is provided as a supplementary file.

IV. CONCLUSION

The design and experimental assessment of a novel mechanism for needle insertions, depicted in Figure 1, have been presented. The experimental results indicate that the mechanism can effectively limit the insertion force and the needle bending by different amounts by appropriate choosing the internal spring, thus, helping to reduce the associated risks. Since the mechanism does not require sensors or actuators, it could be miniaturized and made disposable to suit a wide range of percutaneous procedures, either manual or robotic-assisted, in low-resource settings. Future work will aim to adjust the spring pre-tensioning during the insertion, and will investigate the possibility of adding a tuneable damper. We will also perform a more extensive experimental study considering needles of different geometry, various insertion depths, and different insertion angles in clinically representative conditions.

REFERENCES

[1] I. Jung, K. Han, M. J. Kim, H. J. Moon, J. H. Yoon, V. Y. Park, and E. K. Kim, "Annual trends in ultrasonography-guided 14-gauge core needle biopsy for breast lesions," *Korean Journal of Radiology*, vol. 21, no. 3, pp. 259–267, mar 2020.

[2] K. P. Pritzker and H. J. Nieminen, "Needle biopsy adequacy in the era of precision medicine and value-based health care," *Archives of Pathology and Laboratory Medicine*, vol. 143, no. 11, pp. 1399–1415, nov 2019.

[3] R. J. Jackman and F. A. Marzoni, "Needle-localized breast biopsy: Why do we fail?" *Radiology*, vol. 204, no. 3, pp. 677–684, 1997.

[4] A. D. Li, Y. Liu, J. Plott, L. Chen, J. S. Montgomery, and A. Shih, "Multi-Bevel Needle Design Enabling Accurate Insertion in Biopsy for Cancer Diagnosis," *IEEE Transactions on Biomedical Engineering*, vol. 68, no. 5, pp. 1477–1486, may 2021.

[5] A. Belarouci, S. S. Dhaliwal, M. Sanz-Lopez, F. Verbrugghe, O. Lakhal, T. Chettibi, and R. Merzouki, "Cooperative Brachytherapy Robotic Concept for Localized Cancer Treatment Under Real-Time MRI," *IEEE Transactions on Medical Robotics and Bionics*, vol. 4, no. 3, pp. 667–681, aug 2022.

[6] E. Franco, M. Ristic, M. Rea, and W. M. W. Gedroyc, "Robot-assistant for MRI-guided liver ablation: A pilot study," *Medical Physics*, vol. 43, no. 10, pp. 5347–5356, oct 2016.

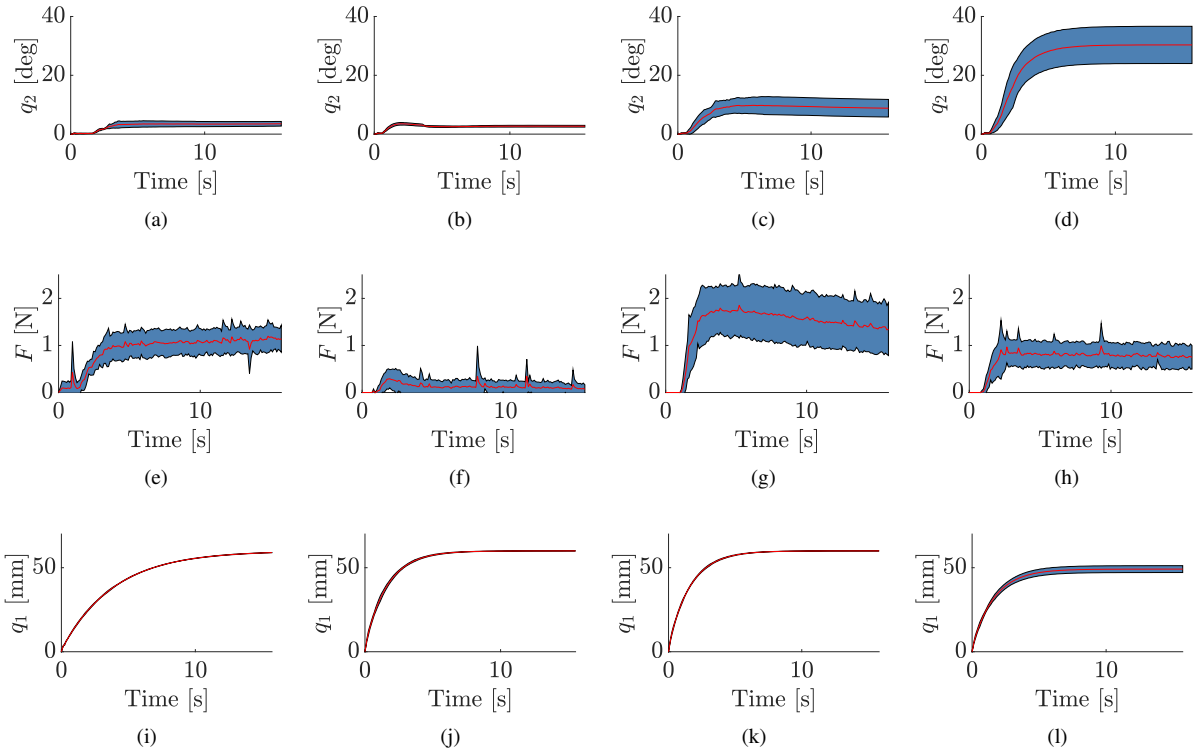

Fig. 3. Test results for Shore A = 10 phantom. **First column -** mean insertion speed 4 mm/s with force-limiting mechanism and Spring 1: (a) bending angle (q_2); (e) insertion force (F); (i) axial displacement (q_1). **Second column -** mean insertion speed 8 mm/s with force-limiting mechanism and Spring 1: (b) bending angle (q_2); (f) insertion force (F); (j) axial displacement (q_1). **Third column -** mean insertion speed 8 mm/s with the force-limiting mechanism and Spring 2: (c) bending angle (q_2); (g) insertion force (F); (k) axial displacement (q_1). **Fourth column -** mean insertion speed 8 mm/s without force-limiting mechanism: (d) bending angle (q_2); (h) insertion force (F); (l) axial displacement (q_1).

[7] B. Zhao, S. Shao, L. Lei, X. Wang, X. Yang, Q. Wang, and Y. Hu, "Curve Fitting-Based Dynamic Path Planning and Tracking Control for Flexible Needle Insertion," *IEEE Transactions on Medical Robotics and Bionics*, vol. 4, no. 2, pp. 436–447, may 2022.

[8] B. Zhao, L. Lei, L. Xu, S. Li, Y. Hu, J. Zhang, X. Yang, and Y. Zhang, "Needle Deflection Modeling and Preoperative Trajectory Planning during Insertion into Multilayered Tissues," *IEEE/ASME Transactions on Mechatronics*, vol. 26, no. 2, pp. 943–954, apr 2021.

[9] C. Avila-Carrasco, M. Ruppel, R. Persad, A. Bahl, and S. Dogramadzi, "Analytical versus Data-Driven Approach of Modelling Brachytherapy Needle Deflection," *IEEE Transactions on Medical Robotics and Bionics*, vol. 2, no. 4, pp. 519–528, nov 2020.

[10] T. Lehmann, C. Rossa, N. Usmani, R. S. Sloboda, and M. Tavakoli, "Intraoperative Tissue Young's Modulus Identification during Needle Insertion Using a Laterally Actuated Needle," *IEEE Transactions on Instrumentation and Measurement*, vol. 67, no. 2, pp. 371–381, feb 2018.

[11] D. A. Lezcano, I. I. Iordachita, and J. S. Kim, "Lie-Group Theoretic Approach to Shape-Sensing Using FBG-Sensorized Needles Including Double-Layer Tissue and S-Shape Insertions," *IEEE Sensors Journal*, nov 2022.

[12] E. Franco, M. Rea, W. Gedroyc, and M. Ristic, "Control of a Master-Slave Pneumatic System for Teleoperated Needle Insertion in MRI," *IEEE/ASME Transactions on Mechatronics*, vol. 21, no. 5, pp. 2595–2600, 2016.

[13] C. Shi, Z. Tang, and S. Wang, "Design and Experimental Validation of a Fiber Bragg Grating-Enabled Force Sensor with an Ortho-Planar Spring-Based Flexure for Surgical Needle Insertion," *IEEE Transactions on Medical Robotics and Bionics*, vol. 3, no. 2, pp. 362–371, may 2021.

[14] T. Zhang, Y. Wen, and Y. H. Liu, "Developing a Parallel Robot for MRI-Guided Breast Intervention," *IEEE Transactions on Medical Robotics and Bionics*, vol. 2, no. 1, pp. 17–27, feb 2020.

[15] M. A. Alamilla, C. Barnouin, R. Moreau, F. Zara, F. Jaillet, H. T. Redarce, and F. Coury, "A Virtual Reality and Haptic Simulator for Ultrasound-Guided Needle Insertion," *IEEE Transactions on Medical Robotics and Bionics*, vol. 4, no. 3, pp. 634–645, aug 2022.

[16] R. Tsumura, J. S. Kim, H. Iwata, and I. Iordachita, "Preoperative Needle Insertion Path Planning for Minimizing Deflection in Multilayered Tissues," *IEEE Robotics and Automation Letters*, vol. 3, no. 3, pp. 2129–2136, jul 2018.

[17] N. Abolhassani, R. V. Patel, and F. Ayazi, "Minimization of needle deflection in robot-assisted percutaneous therapy," *The International Journal of Medical Robotics and Computer Assisted Surgery*, vol. 3, no. 2, pp. 140–148, jun 2007.

[18] C. L. Lin and Y. A. Huang, "Simultaneously Reducing Cutting Force and Tissue Damage in Needle Insertion with Rotation," *IEEE Transactions on Biomedical Engineering*, vol. 67, no. 11, pp. 3195–3202, nov 2020.

[19] A. Donder and F. R. Y. Baena, "Kalman-Filter-Based, Dynamic 3-D Shape Reconstruction for Steerable Needles With Fiber Bragg Gratings in Multicore Fibers," *IEEE Transactions on Robotics*, pp. 1–14, dec 2021.

[20] E. Franco, T. Brown, A. Astolfi, and F. Rodriguez y Baena, "Adaptive energy shaping control of robotic needle insertion," *Mechanism and Machine Theory*, vol. 155, p. 104060, jan 2021.

[21] E. Franco and A. Donaire, "Energy shaping nonlinear control of under-actuated needle insertion," *Control Engineering Practice*, vol. 128, p. 105326, nov 2022.

[22] Y.-Q. Yu, L. L. Howell, C. Lusk, Y. Yue, and M.-G. He, "Dynamic Modeling of Compliant Mechanisms Based on the Pseudo-Rigid-Body Model," *Journal of Mechanical Design*, vol. 127, no. 4, p. 760, jul 2005.

[23] Y. C. Yoon, J. S. Lee, S. U. Park, J. H. Kwon, T. H. Hong, and D. G. Kim, "Quantitative assessment of liver fibrosis using shore durometer," *Annals of Surgical Treatment and Research*, vol. 93, no. 6, pp. 300–304, dec 2017.

[24] D. J. van Gerwen, J. Dankelman, and J. J. van den Dobbelsteen, "Needle-tissue interaction forces–a survey of experimental data." *Medical engineering & physics*, vol. 34, no. 6, pp. 665–80, 2012.

[25] S. J. Elliott, M. G. Tehrani, and R. S. Langley, "Nonlinear damping and quasi-linear modelling," *Philosophical Transactions of the Royal Society A: Mathematical, Physical and Engineering Sciences*, vol. 373, no. 2051, pp. 1–30, sep 2015.